Do Submesoscales Affect the Large-Scale Structure of the Upper Ocean?

ANIRBAN SINHA,[a] JÖRN CALLIES,[a] AND DIMITRIS MENEMENLIS[b]

[a] *California Institute of Technology, Pasadena, California*
[b] *Jet Propulsion Laboratory, Pasadena, California*

(Manuscript received 16 June 2022, in final form 5 November 2022)

ABSTRACT: Submesoscale baroclinic instabilities have been shown to restratify the surface mixed layer and to seasonally energize submesoscale turbulence in the upper ocean. But do these instabilities also affect the large-scale circulation and stratification of the upper thermocline? This question is addressed for the North Atlantic Subtropical Mode Water region with a series of numerical simulations at varying horizontal grid spacings (16, 8, 4, and 2 km). These simulations are realistically forced and integrated long enough for the thermocline to adjust to the presence or absence of submesoscales. Linear stability analysis indicates that a 2-km grid spacing is sufficient to resolve the most unstable mode of the wintertime mixed layer instability. As the resolution is increased, spectral slopes of horizontal kinetic energy flatten and vertical velocities increase in magnitude, consistent with previous regional and short-time simulations. The equilibrium stratification of the thermocline changes drastically as the grid spacing is refined from 16 to 8 km and mesoscale eddies are fully resolved. The thermocline stratification remains largely unchanged, however, between the 8-, 4-, and 2-km runs. This robustness is argued to arise from a mesoscale constraint on the buoyancy variance budget. Once mesoscale processes are resolved, the rate of mesoscale variance production is largely fixed. This constrains the variance destruction by submesoscale vertical buoyancy fluxes, which thus remain invariant across resolutions. The bulk impact of mixed layer instabilities on upper-ocean stratification in the Subtropical Mode Water region through an enhanced vertical buoyancy flux is therefore captured at 8-km grid spacing, even though the instabilities are severely underresolved.

KEYWORDS: Boundary currents; Eddies; Mesoscale processes; Ocean dynamics; Thermocline circulation

1. Introduction

Submesoscale mixed layer baroclinic instability restratifies the upper-ocean mixed layer by turning lateral buoyancy gradients into vertical ones (Boccaletti et al. 2007; Fox-Kemper et al. 2008). In the process, it converts mesoscale potential energy into submesoscale kinetic energy, causing a seasonal modulation of submesoscale energy levels following the seasonal cycle in mixed layer depth (Mensa et al. 2013; Sasaki et al. 2014; Callies et al. 2015, 2016). The long-term and large-scale impacts of these instabilities, however, remain largely unknown.

Much of the recent work on submesoscale turbulence has relied on short integrations of high-resolution models, often in domains of limited size (e.g., Capet et al. 2008; Mensa et al. 2013; Sasaki et al. 2014; Gula et al. 2014; Su et al. 2018; Balwada et al. 2018; Schubert et al. 2020). This work has revealed that submesoscales dominate vertical velocities and the vertical transport of heat and tracers in the upper ocean. In relying on short integrations, however, these studies have effectively treated submesoscale processes as a rapid adjustment problem with no feedback on the large-scale, time-mean state. In the present study, we use longer integrations to assess the impact of submesoscale flows on the upper thermocline in the midlatitude North Atlantic.

This work is motivated by Lévy et al. (2010), who conducted numerical experiments in an idealized North Atlantic basin to investigate such impacts. When increasing the resolution to capture submesoscales, they observed a drastic change in the thermocline stratification, suggesting that submesoscale processes might play a leading-order role in the large-scale dynamics of the thermocline. In these idealized simulations, however, the increase in resolution caused a southward shift of the western boundary current extension, which in turn caused

Sinha's current affiliation: Picarro Inc., Santa Clara, California.

Supplemental information related to this paper is available at the Journals Online website: https://doi.org/10.1175/JPO-D-22-0129.s1.

Corresponding author: Anirban Sinha, as4479@columbia.edu

DOI: 10.1175/JPO-D-22-0129.1

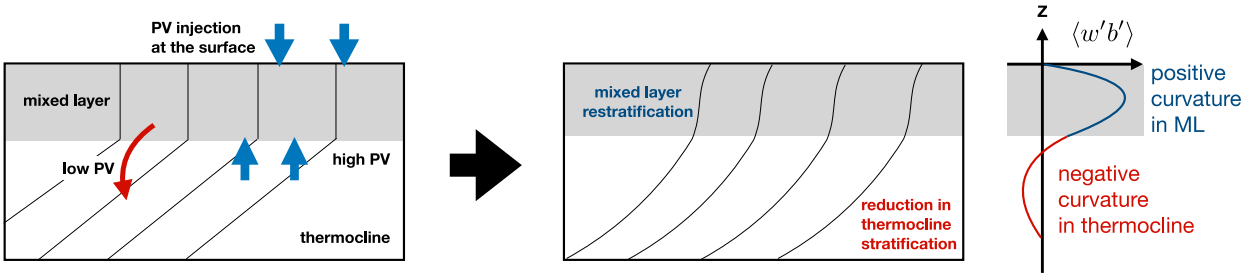

FIG. 1. Impact of submesoscale MLI on the stratification of the upper ocean. MLI generates PV fluxes at the surface, upwells high-PV water from the thermocline into the mixed layer, and subducts low-PV water into the upper thermocline. The vertical buoyancy flux generated by MLI peaks in the mixed layer and is weak and negative below. The stratification tendency is proportional to the curvature of the flux profile, which is positive in the mixed layer and negative below. MLI thus tends to restratify the mixed layer and reduce stratification in the upper thermocline.

the entire warm-water lens of the subtropical gyre to shift southward. It remained unclear whether the observed stratification change was directly attributable to local submesoscale physics.

Our approach here is similar to that of Lévy et al. (2010), but we employ a more realistic setup to capture the topographic control of the real Gulf Stream. We conduct a suite of numerical simulations of the midlatitude North Atlantic using the Massachusetts Institute of Technology general circulation model (MITgcm; Marshall et al. 1997). We use realistic bathymetry, atmospheric forcing, and lateral boundary conditions, and we integrate these simulations over 43 years. Like Lévy et al. (2010), we vary the horizontal resolution to assess the impact of submesoscale flows.

Chassignet and Xu (2017) conducted a similar numerical experiment in the North Atlantic but focused on the kinetic energy and character of the Gulf Stream rather than the stratification. They observed a more realistic Gulf Stream path and structure once they decreased horizontal grid spacing to about 2 km. These simulations did not include the dependence of wind stress on surface currents, which Renault et al. (2016) showed exerts a strong control on the Gulf Stream path. Although this is not the focus of this work, we take this current dependence into account and do not find any strong changes in the Gulf Stream path once mesoscale eddies are resolved (section 3).

A local impact of submesoscale turbulence on the thermocline stratification might be expected because mixed layer instabilities (MLI) produce vertical buoyancy fluxes in both the mixed layer and the upper thermocline. Recent advances in theory (Boccaletti et al. 2007; Fox-Kemper et al. 2008; Callies et al. 2016) and observations (Callies et al. 2015; Thompson et al. 2016; du Plessis et al. 2017, 2019; Taylor et al. 2018; Buckingham et al. 2019; Callies et al. 2020) have clarified the physics of submesoscale flows and MLI (Fig. 1). In winter, due to a combination of surface cooling and wind forcing, the stratification of the surface ocean is eroded and progressively deeper isopycnals start outcropping. This results in a weakly stratified surface mixed layer sitting atop a more strongly stratified thermocline that remains shielded from direct atmospheric forcing. The combination of lateral density gradients and change in stratification at the mixed layer base give rise to opposing quasigeostrophic potential vorticity (PV) gradients at the surface and mixed layer base. The resulting baroclinic instability leads to an injection of high Ertel PV into the mixed layer, both through surface PV fluxes and the upwelling of high-PV thermocline water (cf. Nakamura and Held 1989; Garner et al. 1992). The injection of high PV into the mixed layer results in restratification. As a corollary, however, MLI also subducts low-PV water into the thermocline, which should cause a concurrent reduction in stratification there. While the focus in the literature has largely been on the restratification of the mixed layer (Fox-Kemper et al. 2008), here we highlight the stratification changes in both the mixed layer and the thermocline below.

The reduction in thermocline stratification deserves particular attention in regions of mode water formation such as the western subtropical gyre, where seasonally ventilated mode waters play an important role in the coupling between the atmosphere and interior ocean. The wintertime formation of Subtropical Mode Water (STMW) primarily by surface cooling and subsequent subduction into a layer overlying the main thermocline constitutes an important pathway for heat and freshwater anomalies into the interior ocean (e.g., Worthington 1958; Forget et al. 2011). The ventilation of STMW also plays a key role in the oceanic uptake of anthropogenic CO_2 (Bates et al. 2002; Iudicone et al. 2016) and other biogeochemical processes such as nutrient cycling (Palter et al. 2005). Submesoscale physics have also been suggested to affect the biogeochemical properties of mode waters by causing filamentary subduction in early spring, before the seasonal retreat of the mixed layer (Karleskind et al. 2011).

To understand how the large-scale stratification of the upper ocean is affected by submesoscale eddy fluxes, we consider the horizontally averaged buoyancy budget. The horizontally averaged buoyancy equation can be written as

$$\partial_t \langle b \rangle + \langle \nabla_h \cdot (\mathbf{u} b) \rangle + \partial_z (\langle w \rangle \langle b \rangle) + \partial_z \langle w' b' \rangle = \langle Q \rangle, \qquad (1)$$

where b is buoyancy, $\mathbf{u}$ the velocity vector, $\langle \cdot \rangle$ denotes the horizontal average, and primes denote deviations from the horizontal average (no time mean removed). All nonconservative terms have been grouped together into Q, which includes

the divergence of parameterized buoyancy fluxes, penetrative shortwave radiation, and contributions from the nonlinearity of the equation of state. Differentiating (1) in the vertical, we obtain an evolution equation for the stratification:

$$\partial_t\langle\partial_z b\rangle = \partial_z\langle Q\rangle - \partial_z\langle\nabla_h\cdot(\mathbf{u}b)\rangle - \partial_{zz}(\langle w\rangle\langle b\rangle) - \partial_{zz}\langle w'b'\rangle. \tag{2}$$

The stratification $\langle\partial_z b\rangle$ responds to the curvature of the vertical eddy buoyancy flux profile, $\partial_{zz}\langle w'b'\rangle$. The vertical eddy buoyancy flux is also equal to the conversion rate between potential and kinetic energy (buoyancy production). Converting potential to kinetic energy, MLI produces a positive $\langle w'b'\rangle$ that peaks in the mixed layer, which leads to restratification there: $-\partial_{zz}\langle w'b'\rangle > 0$ (Boccaletti et al. 2007; Fox-Kemper et al. 2008). The buoyancy flux decays below the mixed layer base, which requires a reversal of the curvature and thus implies a tendency to reduce the stratification in the upper thermocline, $-\partial_{zz}\langle w'b'\rangle < 0$, as anticipated by the PV argument above. If MLI becomes stronger, as might be expected when it is increasingly well resolved, the magnitude of $\langle w'b'\rangle$ increases, as does the magnitude of its curvature $\partial_{zz}\langle w'b'\rangle$. Stronger MLI thus causes more rapid restratification in the mixed layer and a stronger reduction in stratification below.

Wenegrat et al. (2018) offered an apparently contrasting perspective on the role of submesoscales on mode waters. They reported that submesoscale processes reduce the rate of PV removal from the mode water by a factor of about 2. MLI constitutes a net source of PV for the upper ocean and therefore increases the mode water stratification. This finding is not necessarily in conflict with the argument presented above, however, because Wenegrat et al. (2018) constructed a bulk stratification budget extending from the surface down to the base of the mode water, in which only surface PV fluxes enter. Here, we are also interested in the PV exchange between the mixed layer and the thermocline. Stronger MLI increases both the surface injection of PV and the PV flux from the thermocline into the mixed layer.

Despite these expectations for the impact of submesoscales on the stratification of the upper thermocline, the simulations presented here show that the mode water stratification is robust to changes in the model resolution once mesoscale eddies are resolved. Even though submesoscale turbulence becomes increasingly energetic as the grid spacing is reduced, the thermocline stratification remains largely invariant. We argue below that this is the result of a mesoscale constraint on the buoyancy variance that submesoscale MLI feeds on.

The paper is organized as follows. In sections 2 and 3, we describe the model setup and assess the simulations' realism by comparing them to observations. In section 4, we describe the expectations for MLI in these simulations based on linear stability theory. In section 5, we describe the main result, the robustness of thermocline stratification to submesoscale processes. We offer an explanation in section 6, discuss the result's relation to previous work in section 7, and summarize conclusions in section 8.

2. Model setup

We set up a suite of regional simulations at varying horizontal grid spacings (16, 8, 4, and 2 km) in the North Atlantic, spanning the latitudes 26°–43°N, using the MITgcm in hydrostatic mode (Fig. 2). The domain is chosen to include the northern half of the subtropical gyre, which is of importance for mode water formation. The southern edge of the domain is chosen to reduce the computational expense and to pin both the entry point and transport of the Gulf Stream, which helps simulate a realistic Gulf Stream path and thereby fix the location of the northernmost outcropping of mode water isopycnals. Despite these constraints, however, the domain is large enough for eddy fluxes to change the large-scale structure of the thermocline, as demonstrated below. All four simulations have 100 vertical levels, with a grid spacing that is uniform at 5 m in the top 100 m and then expands gradually to 50 m at 1000-m depth and 230 m in the abyss. The vertical resolution does not restrict the development of wintertime MLI and is held fixed across all four simulations. Each simulation is integrated for 43 years, with time steps of 300 s for the 16-km simulation, 200 s for the 8- and 4-km simulations, and 80 s for the 2-km simulation.

The simulations are forced with identical hourly atmospheric fields from the ERA5 reanalysis (Hersbach et al. 2020). The fields from July 2008 to June 2009 are looped to create extended forcing without any interannual variability. The jump is placed in boreal summer, when the winds over the North Atlantic simulation domain are weak and the discontinuity small. Initial as well as boundary conditions at the northern and southern edges of the domain and at the Strait of Gibraltar are imposed for the horizontal velocities (u, v), potential temperature (θ), and salinity (S). These were extracted from the Arctic Subpolar Gyre State Estimate (ASTE; Nguyen et al. 2021) and interpolated onto the model grid for each of the four simulations. The same repeat year as for the atmospheric forcing is used. Although likely inconsequential for this study, tides are forced by imposing barotropic tidal velocities at the boundaries and applying a tidal potential within the domain. The boundary conditions use the amplitudes and phases from TPXO8,[1] extracted using the Oregon State University tidal model driver.[2] The tidal potential is calculated at hourly intervals from the orbital position of the sun and moon, obtained using NASA's SPICE software, and is corrected for the solid-Earth tide.[3] Time-mean river runoff is from Large and Nurser (2001) as processed by Stammer et al. (2004). The bottom topography is taken from Smith and Sandwell SRTM15 + V2,[4] bin-averaged onto the respective model grids. Lakes and rivers are filled in to prevent numerical instabilities in shallow waters.

Vertical mixing is parameterized using the K-profile parameterization (KPP; Large et al. 1994). Shear is smoothed horizontally with a 121 filter to avoid the generation of gridscale

[1] https://www.tpxo.net/global/tpxo8-atlas.
[2] https://www.esr.org/research/polar-tide-models/tmd-software/.
[3] https://github.com/joernc/tidal-potential.
[4] https://topex.ucsd.edu/WWW_html/srtm15_plus.html.

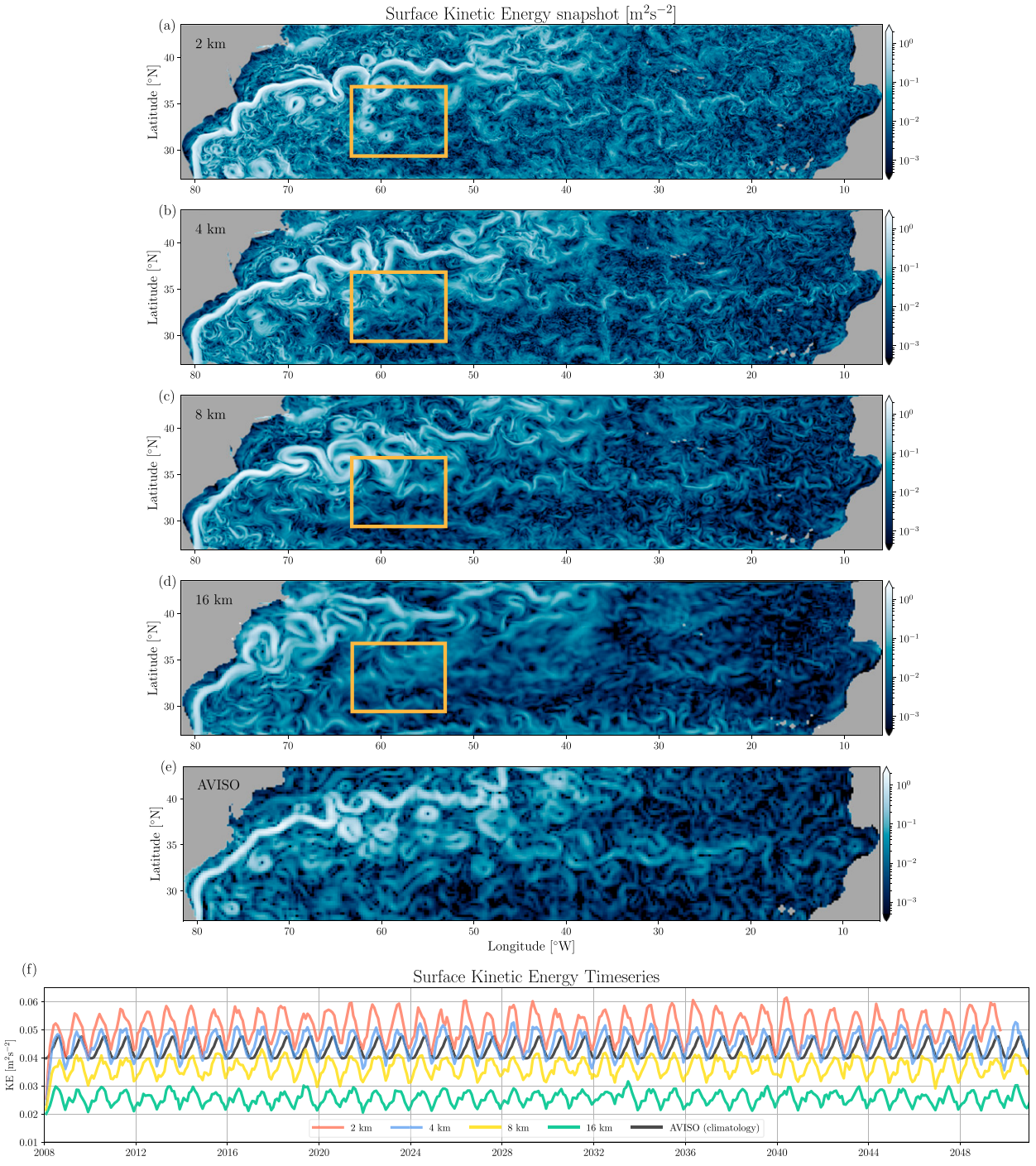

FIG. 2. Simulation domain and surface kinetic energy. (a)–(d) Snapshots of wintertime (15 Feb 2048) surface kinetic energy density from the simulations with 2-, 4-, 8-, and 16-km grid spacing. (e) Equivalent snapshot estimated from altimetry (AVISO, 15 Feb 2009). (f) Time series of domain-averaged, monthly mean surface kinetic energy density for all simulations and altimetry (climatology from 1993 to 2017 data).

patterns in KPP mixing. For all model runs, we use biharmonic horizontal viscosities with Leith and modified-Leith coefficients set to 2 (Fox-Kemper and Menemenlis 2008), a maximum grid-dependent biharmonic viscosity set to 0.8, background vertical eddy diffusivity and viscosity of 10^{-5} and 5×10^{-4} m^2 s^{-1}, respectively, implicit vertical diffusion, and a quadratic bottom drag coefficient of 2×10^{-3}. The model uses the nonlinear equation of state of Jackett and McDougall (1995) with a reference pressure that is a function of depth only. Tracer transport equations for θ and S are solved using

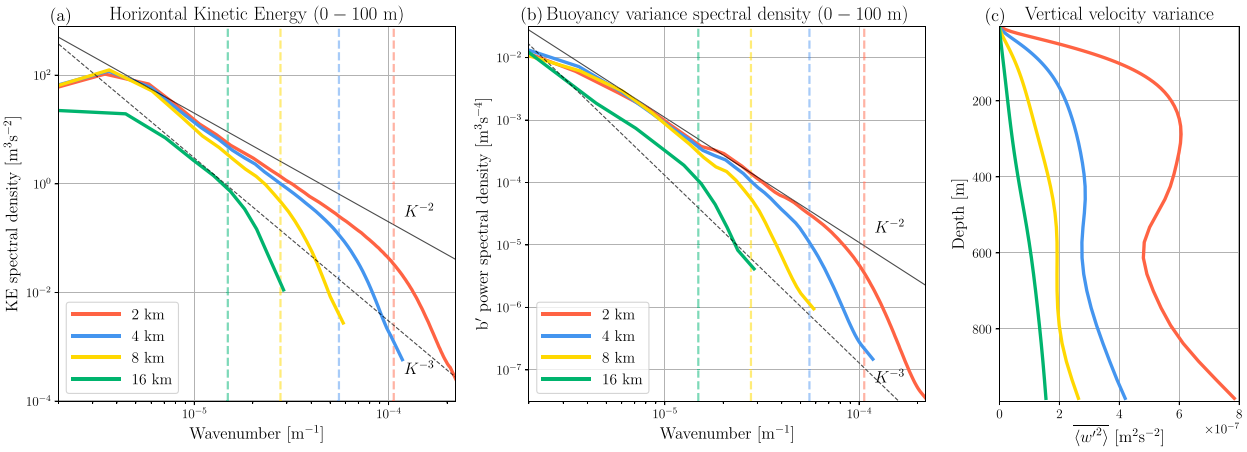

FIG. 3. Successive energization of submesoscales as the resolution is increased. (a) Azimuthally averaged horizontal wavenumber spectra of kinetic energy in the top 100 m. (b) Azimuthally averaged horizontal wavenumber spectra of buoyancy variance in the top 100 m. (c) Profiles of vertical velocity variances $\overline{\langle w'^2 \rangle}$. All statistics are calculated for the analysis domain marked in Fig. 2.

a high-order monotonicity-preserving scheme (Daru and Tenaud 2004) with flux limiter. There is no explicit lateral diffusion.

3. Model evaluation

We examine the surface horizontal velocities in the four simulations (Figs. 2a–d). We compare snapshots of the wintertime (February) surface kinetic energy density 43 years after initialization, when both the thermocline stratification and the mesoscale eddy field have equilibrated, to a snapshot from altimetry (AVISO mapped product,[5] Fig. 2e). These maps reveal that the simulated Gulf Stream follows a realistic path in all but the 16-km simulation. As the resolution is increased, increasingly fine-scale motions appear, indicating increasingly energetic submesoscale turbulence.

Time series of the domain-averaged surface kinetic-energy density show an initial adjustment over a 1–2-yr period before the simulations settle into a statistical equilibrium (Fig. 2f). (The thermocline stratification equilibrates more slowly, as discussed in section 5.) The surface kinetic energy has a marked seasonality in all simulations and in the observations. Both the time-mean kinetic energy and the amplitude of the seasonal cycle increase with resolution. The surface kinetic energy of the 4-km simulation is most similar to the AVISO observational estimate, whereas the surface kinetic energies of the 2- and 8-km simulations are slightly higher and lower than AVISO, respectively. Note, however, that the AVISO mapped product captures neither scales below ~200 km nor ageostrophic motions. The surface kinetic energy of the 16-km simulation is substantially lower than AVISO's, suggesting that mesoscale eddies are underresolved.

To more quantitatively assess the impact of resolution on different scales of motion, we compute azimuthally averaged horizontal wavenumber spectra of the near-surface kinetic energy (0–100-m depth, Fig. 3a) and buoyancy variance (b'^2, Fig. 3b). We calculate these spectra over a region south of the Gulf Stream extension and away from the southern domain boundary (orange box in Fig. 2), where the flow statistics are approximately homogeneous and deep mixed layers and energetic mesoscale eddies produce strong MLI. The mode water layer has an average thickness of about 250 m in this analysis domain, although the location of thickest mode water shifts from the center of the analysis domain in the 16-km run to its northeast corner in the other three runs (Fig. S1 in the online supplemental material). We use two years of 4-hourly snapshots from the final two years of the 43-yr simulations.[6] Consistent with previous work (e.g., Capet et al. 2008; Chassignet and Xu 2017; Sasaki et al. 2017), these spectra show that submesoscales are progressively energized as resolution is increased. The spectra from all experiments have a peak around a wavelength of 300 km. This mesoscale peak has significantly less power in the 16-km simulation compared to the other three cases, again indicating that mesoscale eddies are not fully resolved with 16-km horizontal grid spacing. For the other three simulations (8, 4, and 2 km), the mesoscale part of the spectrum remains fixed but the spectral power at submesoscales progressively increases as additional submesoscale flows are resolved. The spectra for each simulation drop off steeply at length scales smaller than roughly 4–5 times the grid spacing, which we thus identify as the effective resolution (marked by dashed vertical lines in Fig. 3a). Horizontal wavenumber spectra of buoyancy variance show a similar resolution dependence (Fig. 3b).

Also consistent with previous work (e.g., Capet et al. 2008), we find a dramatic increase in vertical velocities as the grid is refined (Fig. 3c). We calculate the variances $\overline{\langle w'^2 \rangle}$ from the

[5] https://cds.climate.copernicus.eu/cdsapp#!/dataset/satellite-sea-level-global?tab=overview.

[6] These spectral calculations were carried out using the xrft Python package (https://github.com/xgcm/xrft).

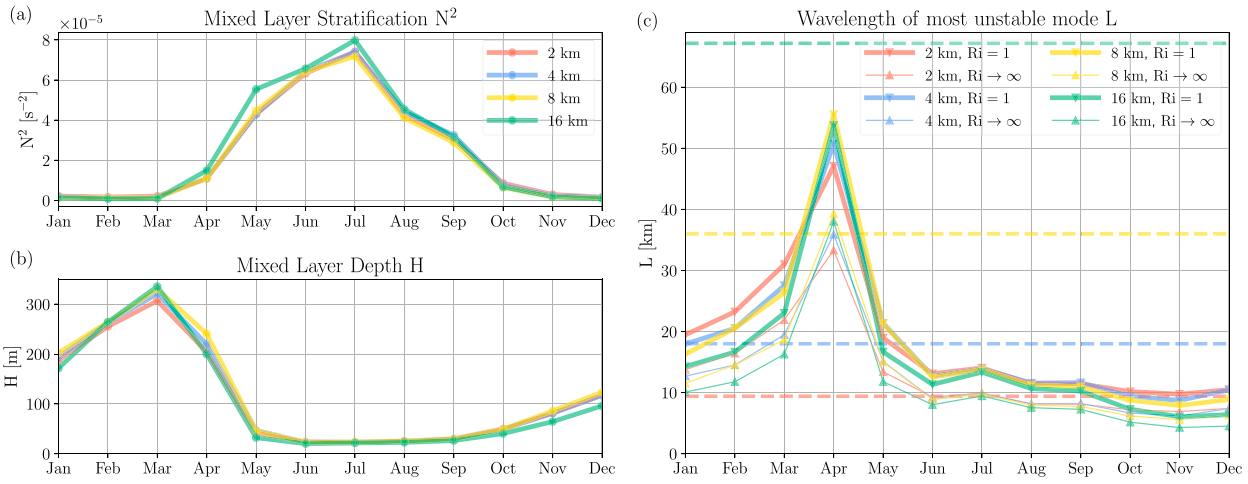

FIG. 4. Mixed layer instability scales. (a) Climatology of stratification N^2 in the mixed layer. (b) Climatology of mixed layer depth H. (c) Climatology of the resulting scale of the most unstable mixed layer mode, calculated using (3) with Ri = 1 and Ri → ∞ (the quasigeostrophic limit). The dashed lines indicate the effective resolution of each simulation (same as in Figs. 3a,b).

same two years of 4-hourly snapshots used above. A maximum in vertical velocity variance emerges within the winter mixed layer. At 200 m, the variance increases from 2.7×10^{-8} m^2 s^{-2} for the 16-km grid to 5.7×10^{-7} m^2 s^{-2} for the 2-km grid. As the grid spacing is reduced, the variance also increases in the permanent thermocline, which we attribute to the resolution of higher-frequency internal waves (cf. Garrett and Munk 1972).

In summary, the 8-, 4-, and 2-km simulations equilibrate to a statistically steady state with a reasonable Gulf Stream path and a realistic mesoscale eddy field. Submesoscale turbulence is progressively energized as the horizontal grid spacing is reduced and exhibits a phenomenology consistent with previous work. In the following sections, we examine how the thermocline stratification responds to these increasingly energetic submesoscale flows.

4. Instability scales

To understand to what degree the different simulations resolve MLI, we estimate the wavelength of the most unstable mixed layer mode using Stone's (1966) formula

$$L = \sqrt{\frac{\mathrm{Ri} + 1}{\mathrm{Ri}}}\frac{2\pi}{1.6}\frac{NH}{f}, \tag{3}$$

where Ri is the Richardson number of the mixed layer, N is the mixed layer buoyancy frequency, H is the mixed layer depth, and f is the inertial frequency. The square root factor provides a correction from the quasigeostrophic limit Ri → ∞ (Eady 1949). We estimate a monthly climatology of this instability scale for each of the four simulations. In a well-resolved simulation, the buoyancy production is concentrated around the instability scale (e.g., Brüggemann and Eden 2015), so resolving it is a sufficient (if not necessary) condition to capture the buoyancy flux of MLI and the submesoscale turbulence it produces.

For a typical mixed layer Ri, the nonquasigeostrophic correction factor does not change the result much. Symmetric and inertial instabilities rapidly restore the mixed layer to Ri = 1, which can thus be considered a lower bound. The correction factor then varies between 1.4 for Ri = 1 and unity in the quasigeostrophic limit. Instead of diagnosing Ri from the model, we present both these bounds.

To estimate the mixed layer stratification, we vertically average $\partial_z b$ over the local and concurrent mixed layer, then we average over the analysis area (orange box in Fig. 2) and over time (2 years of 4-hourly snapshots). We define the mixed layer depth as the depth at which the stratification $\partial_z b$ starts deviating from its surface value by more than 5%. We do not define these quantities using the KPP boundary layer, which is generally deeper and includes a layer of strong stratification at its base. Our definitions thus favor weak stratification and small mixed layer depths, producing conservative estimates of the instability scale. The resulting mixed layer stratification varies between 1.5×10^{-6} and 8×10^{-5} s^{-2} (Fig. 4a), and the resulting mixed layer depth varies between 20 m in summer and 300 m in winter (Fig. 4b). There is not much difference between the four simulations.

The resulting instability scale varies between 10 and 50 km for Ri = 1 and between 7 and 35 km for Ri → ∞ (Fig. 4c). The instability scale peaks in April, when the mixed layer is still deep (~200 km) but has started to stratify. Our estimates are comparable to those of Dong et al. (2020), who estimated the most unstable MLI modes globally from Argo observations and model simulations.

In the previous section, we estimated the effective resolution to be 4–5 times the grid spacing. The 16-km simulation does not resolve the most unstable mode of MLI at any time of the year. The peak instability scale is comparable to the effective resolution of the 8-km simulation, suggesting that this simulation does not resolve this mode for most of the year. Wintertime MLI is starting to be resolved in the 4-km

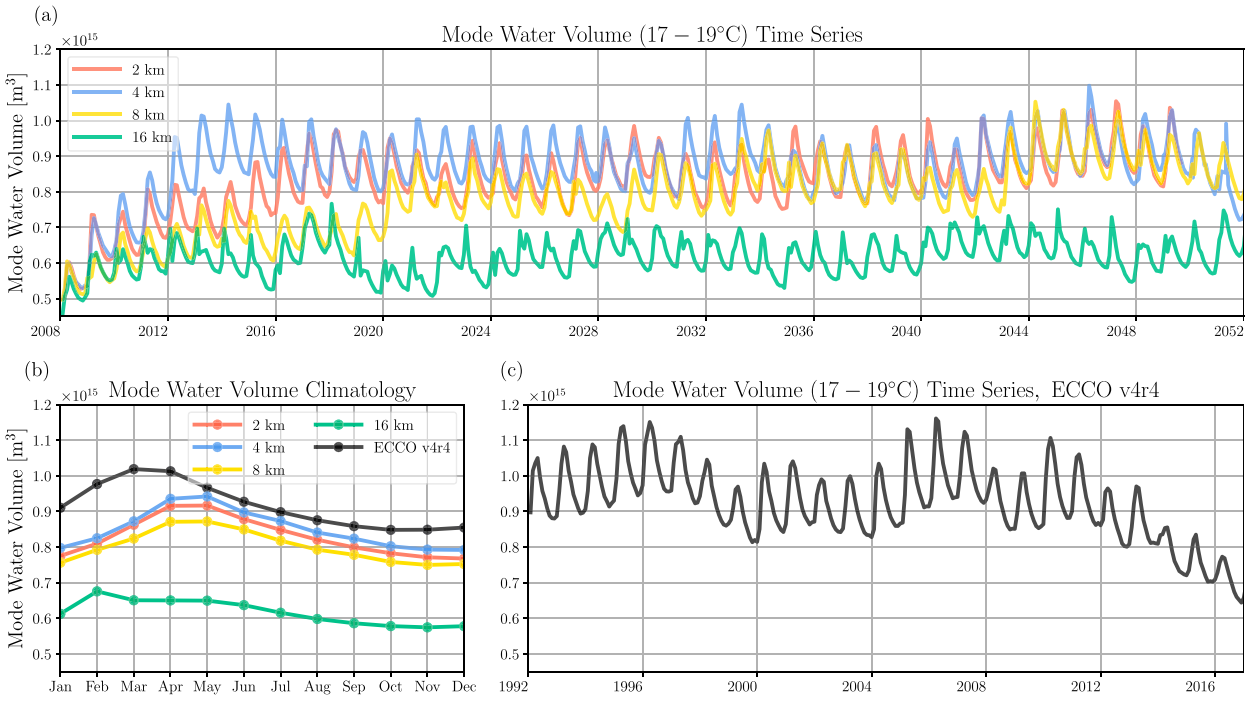

FIG. 5. Simulated and observed mode water volumes. (a) Time series of simulated mode water volume, defined as the volume contained between the 17° and 19°C isotherms west of 40°W. (b) Climatology of the mode water volume obtained from the final 30 years of simulation and from the ECCO state estimate (1992–2017). (c) Time series of mode water volume in the ECCO state estimate.

simulation, but only marginally so. The 2-km simulation resolves the most unstable mode throughout winter and marginally resolves it for the rest of the year.

Our suite of simulations thus ranges from not resolving MLI at all to resolving it well—at least during the winter months, when it is strongest and contributes the bulk of the annual-mean buoyancy fluxes.[7] One might thus expect that MLI becomes progressively stronger as the resolution is increased, an expectation that is consistent with the progressive energization of submesoscales and the diagnosed increase in vertical velocities described in the previous section. As discussed in what follows, however, the improved resolution of MLI does not lead to an increase in the vertical buoyancy flux $\langle w'b' \rangle$ and thus does not affect the stratification of the upper thermocline.

5. Thermocline stratification

We now assess how the stratification of the thermocline responds to the increase in resolution, with a focus on the mode water layer. We define the mode water volume as that contained between the 17° and 19°C isotherms (based on potential temperature) west of 40°W and within the model domain (north of 26°N). This temperature range is a conventional definition for STMW in the region, which is commonly referred to as "Eighteen Degree Water" (e.g., Worthington 1958; Kwon and Riser 2004). The volume of this layer equilibrates within 10–15 years, as can be seen in time series of mode water volume (Fig. 5a). We note that the transient increase in mode water volume is not ordered by resolution—the volume in the 4-km run increases more rapidly than in both the 2- and 8-km runs—which is likely due to intrinsic variability. Even after this initial adjustment period has concluded by nominal year 2022 (Fig. 5a), all runs exhibit considerable interannual to decadal variability. Since the atmospheric forcing is a repeat year, this variability is entirely intrinsic and presumably suppressed compared to that of the real ocean, which also responds to interannual to decadal changes in the atmospheric forcing. The mode water volume exhibits an expected seasonal cycle (Figs. 5a,b): driven by mode water formation during winter, the volume peaks in early spring, and then it declines during summer and fall as mode waters are eroded.

Strikingly, the simulated mode water expands by about 30% as the grid spacing of the simulations is decreased from 16 to 8 km, but there is no substantial change in mode water volume as the grid spacing is further decreased to 4 and 2 km (Figs. 5a,b). The mode water volume is sensitive to whether or not mesoscale eddies are fully resolved (cf. Marshall 1997; Marshall et al. 2002), but it is not sensitive to the resolution of submesoscale MLI. This result is in stark contrast to Lévy et al. (2010), who found a comparable change in the thermocline structure when refining the grid from mesoscale- to

[7] There is some arbitrariness in choosing the effective resolution scales, but this conclusion is robust to somewhat more conservative choices. Wintertime MLI is comfortably resolved by the 2-km simulation.

submesoscale-resolving as when refining it from coarse to mesoscale resolving.

The difference in mode water volume between the 16- and 8-km simulations demonstrates that our domain is large enough to allow for local eddy dynamics to affect the thermocline structure. In other words, the stratification in the interior of the domain is not strongly constrained by the lateral boundary conditions. This is expected because, with the exception of the western boundary current, the wind-driven gyre circulation is southeast to southwestward, and characteristics are directed from the outcrop positions within the domain toward the boundary (Luyten et al. 1983). The southern boundary conditions thus influence only a thin layer adjacent to the boundary (except where the Florida Current enters the domain).

The mode water volume is more realistic in the 8-, 4-, and 2-km simulations than in the 16-km simulation (Fig. 5). We evaluate the realism of our simulations using the ECCO v4r4 state estimate (Fukumori et al. 2020). The mode water volume in ECCO exhibits substantial interannual and decadal variability, which spans the range of simulated volumes in the 8-, 4-, and 2-km simulations (after the initial adjustment). The climatological volume, averaged over the final 30 simulation years, is 10%–20% too low compared to the long-term observed average (1992–2017) and the simulated seasonal peak is a month too late (Fig. 5b). This level of disagreement between the 8-, 4-, and 2-km simulations and observations is not unexpected, given that the atmospheric forcing during the repeat year (July 2008–June 2009) does not coincide with the long-term climatology. By contrast, the 16-km simulation has a volume that is much smaller than observed and a seasonal cycle that is clearly too weak (Fig. 5).

Similarly, meridional sections across the mode water show that the 8-, 4-, and 2-km simulations have a comparable and realistic time-mean thermal structure, whereas the 16-km simulation is markedly different (Fig. 6). At representative sections (67°, 64°, 55°, and 52°W), the 17° and 19°C isotherms roughly align between the 8-, 4-, and 2-km simulations but differ in the 16-km simulation (Figs. 6b–e). Especially in the two eastern sections, the isotherms in the latter simulation are too shallow and too close together. In the two western sections, there are some differences between the 8-km simulation, on the one hand, and the 4-and 2-km simulations, on the other, but overall the consistency between the three high-resolution simulations is much greater than with the 16-km run. This consistency between the 8-, 4-, and 2-km simulations and the discrepancy with the 16-km simulation holds more generally for the thermal structure of the upper ocean (Figs. 6f–j). The 16-km simulation has mode water that is too cold, capped by stratification that is too strong.

6. A mesoscale constraint

The proximate cause for the thermocline structure remaining largely invariant when submesoscale MLI is increasingly well resolved is that the vertical buoyancy flux does not change much between the 8-, 4-, and 2-km simulations (Fig. 7e). As discussed in the introduction, it would have been through an increase in the vertical buoyancy flux that one might have expected MLI to affect the stratification in the upper thermocline. That this flux remains largely constant is remarkable, given that MLI is severely underresolved with 8-km grid spacing (Fig. 4) and that vertical velocities substantially increase in magnitude as the resolution is increased (Fig. 3b). Furthermore, the vertical buoyancy flux is carried by increasingly small scales as they come to be resolved (Figs. 7a–d)—yet, the spectral integral does not change much (Fig. 7e).

To explain this behavior—a large change in the vertical buoyancy flux when mesoscale eddies are fully captured but little change as more of the submesoscale range is resolved—we turn to the buoyancy variance budget. We argue that the submesoscale buoyancy flux is tightly constrained by mesoscale processes.

To derive a budget for eddy buoyancy variance, we split the buoyancy field in our analysis domain (Fig. 2) into a background stratification, a component accounting for time-mean, domain-averaged horizontal gradients, and deviations:

$$b = \int^{z} N^2(z')\,dz' + \boldsymbol{\Gamma}\cdot\mathbf{x} + \tilde{b} \quad \text{with} \quad N^2 = \overline{\langle \partial_z b\rangle} \quad \text{and} \quad \boldsymbol{\Gamma} = \overline{\langle \nabla_h b\rangle} \tag{4}$$

Here, $\langle\cdot\rangle$ is a horizontal average over the analysis domain, $\overline{\cdot}$ denotes a time average, and $\mathbf{x}$ is the position vector referenced to the center of the analysis domain. Both N^2 and $\boldsymbol{\Gamma}$ are functions of z only, so the buoyancy budget can be written as

$$\partial_t \tilde{b} + \mathbf{u}\cdot\nabla\tilde{b} + \mathbf{u}\cdot\boldsymbol{\Gamma} + wN^2 = Q, \tag{5}$$

and the buoyancy anomaly $\tilde{b}' = \tilde{b} - \langle\tilde{b}\rangle$ satisfies the equation

$$\partial_t \tilde{b}' + \mathbf{u}\cdot\nabla\tilde{b} - \langle\mathbf{u}\cdot\nabla\tilde{b}\rangle + \mathbf{u}'\cdot\boldsymbol{\Gamma} + w'N^2 = Q', \tag{6}$$

where $\mathbf{u}' = \mathbf{u} - \langle\mathbf{u}\rangle$ and $Q' = Q - \langle Q\rangle$ are the anomalies of the flow and nonconservative tendencies. Multiplying (6) by $\tilde{b}'$ and horizontally averaging over the analysis domain then yields the buoyancy variance budget

$$\partial_t \frac{1}{2}\langle\tilde{b}'^2\rangle + \langle\mathbf{u}\tilde{b}'\cdot\nabla\tilde{b}\rangle + \langle\mathbf{u}'\tilde{b}'\rangle\cdot\boldsymbol{\Gamma} + N^2\langle w'\tilde{b}'\rangle = \langle\tilde{b}'Q'\rangle, \tag{7}$$

which with $\nabla\tilde{b} = \langle\partial_z\tilde{b}\rangle + \nabla\tilde{b}'$ and upon time-averaging becomes (in equilibrium)

$$\overline{\langle\mathbf{u}\cdot\nabla\frac{1}{2}\tilde{b}'^2\rangle} + \overline{\langle\mathbf{u}'\tilde{b}'\rangle}\cdot\boldsymbol{\Gamma} + \overline{(N^2 + \langle\partial_z\tilde{b}\rangle)\langle w'\tilde{b}'\rangle} = \overline{\langle\tilde{b}'Q'\rangle}. \tag{8}$$

This equation, if divided by N^2, is similar to the budget of eddy available potential energy in quasigeostrophic dynamics. The only difference in the primitive equation system is that the advection in the second term on the left includes vertical advection, and that $\langle w'\tilde{b}'\rangle$ is multiplied by a factor that accounts for the deviations of the horizontally averaged stratification from N^2. The first term on the left represents the advective import or export of buoyancy variance across the domain boundaries plus vertical redistribution, the second term on the left represents the production of buoyancy variance by stirring of the horizontally averaged buoyancy gradient

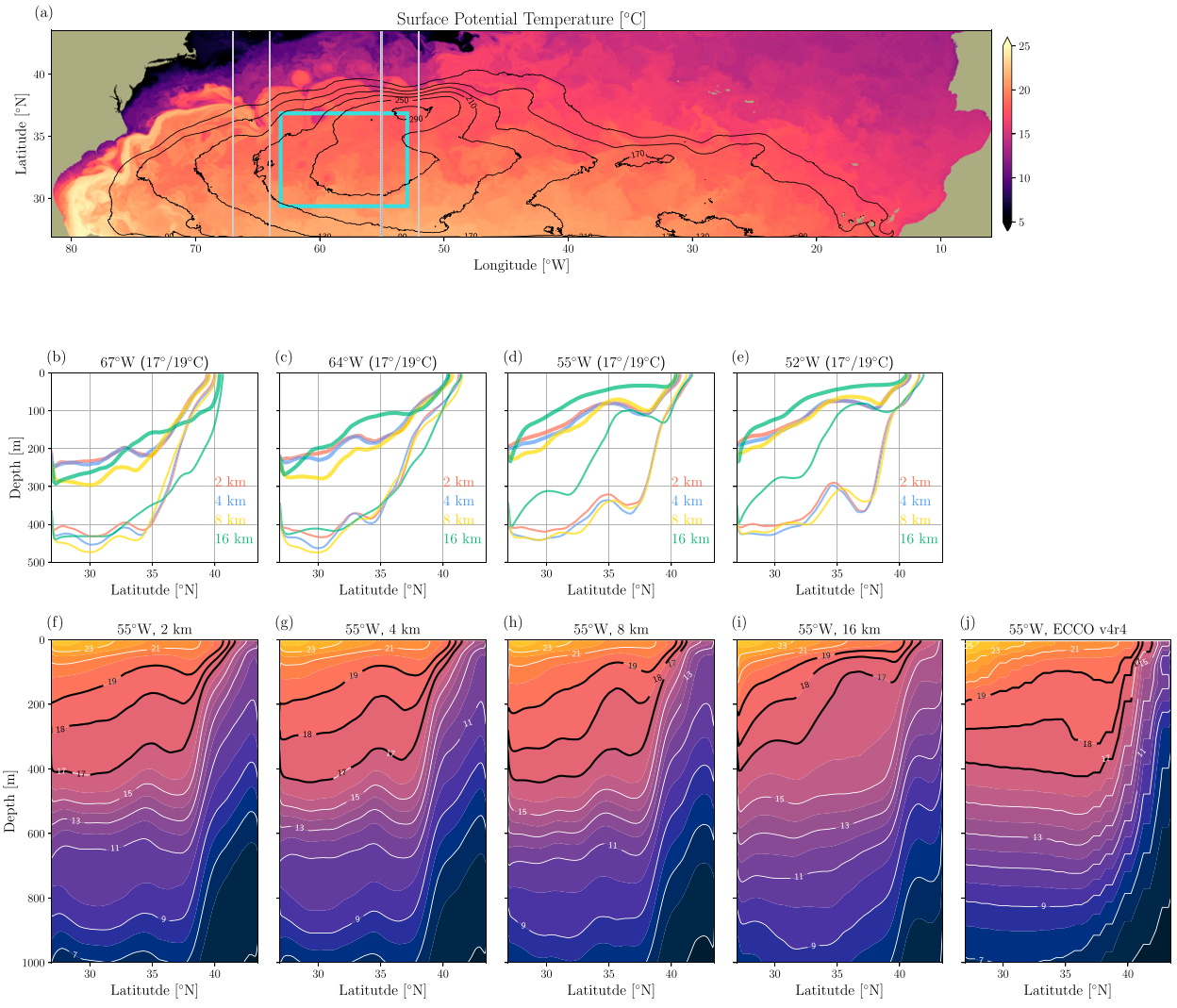

FIG. 6. Simulated and observed thermal structure of the upper ocean. (a) Snapshot of surface potential temperature from the 2-km simulation, with contours showing the mean mode water thickness and the box showing the analysis domain. (b)–(e) Depths of the time mean 17° and 19°C isotherms in the four simulations (averaged over the final 30 years of simulation) along the sections marked by gray lines in (a). (f)–(j) Full potential-temperature fields in the top 1000 m along the section at 55°W for all four simulations and as estimated by ECCO (averaged from 1992 to 2017).

$\boldsymbol{\Gamma}$, and the third term on the left represents the destruction of buoyancy variance by typically positive vertical buoyancy fluxes that act on typically stable stratification. The term on the right represents buoyancy variance production or destruction by nonconservative processes and is typically negative.

From the budget (8), it can be argued that large changes in $\langle w'\tilde{b}'\rangle$ are impossible once mesoscale eddies are resolved. The dominant balance is between $\overline{\langle \mathbf{u}\cdot[\nabla(1/2)\tilde{b}'^2]\rangle} + \overline{\langle \mathbf{u}'\tilde{b}'\rangle}\cdot\boldsymbol{\Gamma}$ and $\overline{(N^2+\langle\partial_z\tilde{b}\rangle)\langle w'\tilde{b}'\rangle}$ (Figs. 8, 9). The first two terms are dominated by mesoscale processes: the propagation of mesoscale eddies into the domain and mesoscale stirring of the large-scale buoyancy gradient. As the grid spacing is decreased below 8 km, $\overline{\langle \mathbf{u}\cdot[\nabla(1/2)\tilde{b}'^2]\rangle} + \overline{\langle \mathbf{u}'\tilde{b}'\rangle}\cdot\boldsymbol{\Gamma}$ remains roughly constant because mesoscale eddies are already well resolved at 8 km (Fig. 8c). If the balance is to be maintained, $\overline{(N^2+\langle\partial_z\tilde{b}\rangle)\langle w'\tilde{b}'\rangle}$ must also remain the same (Fig. 8d). To allow for an increase of $\langle w'\tilde{b}'\rangle$ in the mixed layer, we would then need an attendant decrease in the stratification $N^2+\langle\partial_z\tilde{b}\rangle$. But an increased $\langle w'\tilde{b}'\rangle$ in the mixed layer would do just the opposite: it would tend to *increase* the stratification. The mesoscale production of eddy buoyancy variance thus imposes a strong constraint on the size of $\langle w'\tilde{b}'\rangle$.

This constraint appears to be so strong that it allows the 8-km simulation to have the correct $\langle w'\tilde{b}'\rangle$, despite severely underresolving MLI. The buoyancy flux is carried by unrealistically large scales, but the constraint demands that the spectral

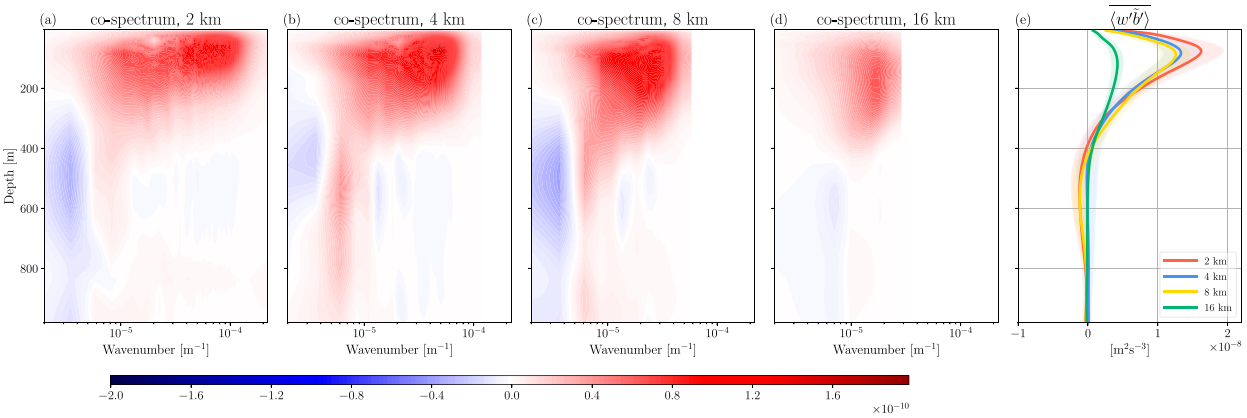

FIG. 7. Vertical buoyancy flux and its spectral decomposition. (a)–(d) Azimuthally averaged cospectra of w' and $\tilde{b}'$ in the top 1000 m, averaged over the final 2 years of simulation. The cospectra are multiplied by the wavenumber to compensate for logarithmic shrinking. (e) Profiles of vertical buoyancy flux $\langle w'\tilde{b}'\rangle$. The shading shows the standard error of the estimation ($\pm 1\sigma$), based on the standard deviation of the domain-averaged fluxes and assuming 25 degrees of freedom.

integral be the same as in the 2- and 4-km simulations (Fig. 7). Only when the mesoscale production of buoyancy variance is underresolved, as it is in the 16-km simulation, does $\langle w'\tilde{b}'\rangle$ change substantially.

The nonconservative term in (8) is not negligible in the upper 50 m or so, but it does not break the mesoscale constraint. It is dominated by small-scale buoyancy variance dissipation and is negative. It would have to decrease in magnitude to compensate for an increase in $\langle w'\tilde{b}'\rangle$. Instead, the dissipation slightly increases as mesoscale eddies are resolved and then remains largely constant (Fig. 8e). Even with severely underresolved MLI, the mesoscale buoyancy variance production is balanced primarily by vertical fluxes working against the mean stratification, not by a nonconservative sink.

7. Contrast to previous work

Our finding that the upper-ocean stratification is largely invariant once mesoscale eddies are resolved stands in contrast to the conclusions drawn by Wenegrat et al. (2018). They argued that when the grid is refined to capture submesoscale fronts, the surface PV injection increases, which in turn causes a net increase in stratification in the upper ocean. They further contended that this result is expected if the surface PV flux scales with $\langle|\nabla b|^2\rangle$, which they rationalized with a scaling argument for the frictional and diabatic components of the PV flux. As the resolution is increased, surface buoyancy gradients are allowed to become sharper and sharper, and thus the PV injection and bulk upper-ocean stratification increase in lockstep with the resolution.

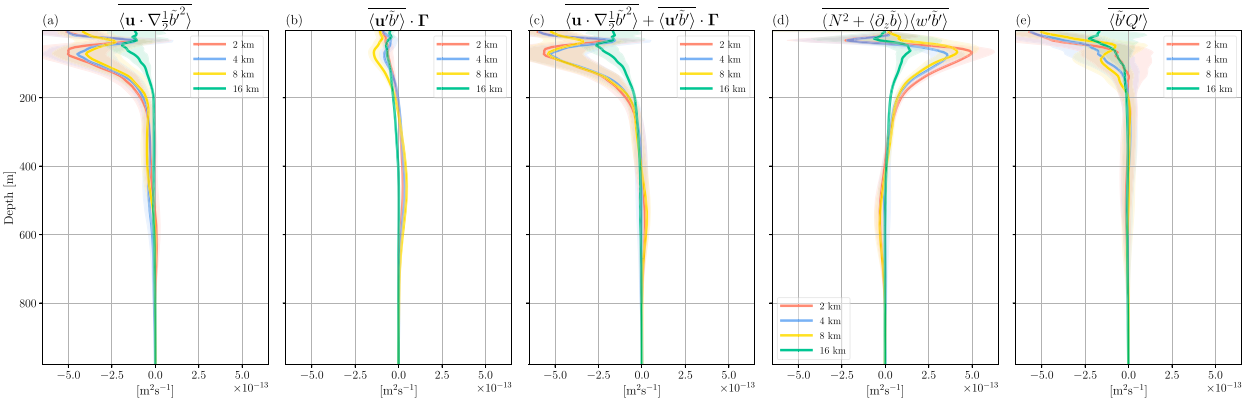

FIG. 8. Buoyancy variance budget. The panels show profiles of the terms in (8) for the analysis domain marked in Fig. 2. (a) Import/export of buoyancy variance budget across the boundaries of the analysis domain. (b) Production of buoyancy variance by horizontal fluxes down the large-scale buoyancy gradient $\mathbf{\Gamma}$. (c) Sum of the first two terms, representing the total mesoscale source of buoyancy variance. (d) Destruction of buoyancy variance by vertical fluxes against the stratification. (e) Buoyancy variance destruction by nonconservative terms, calculated as the residual in (8). All terms are calculated from the final 2 years of the simulations. The shading shows the standard error of the estimation ($\pm 1\sigma$), calculated from the standard deviations of the domain averages and assuming 25 degrees of freedom for the 2-yr analysis period.

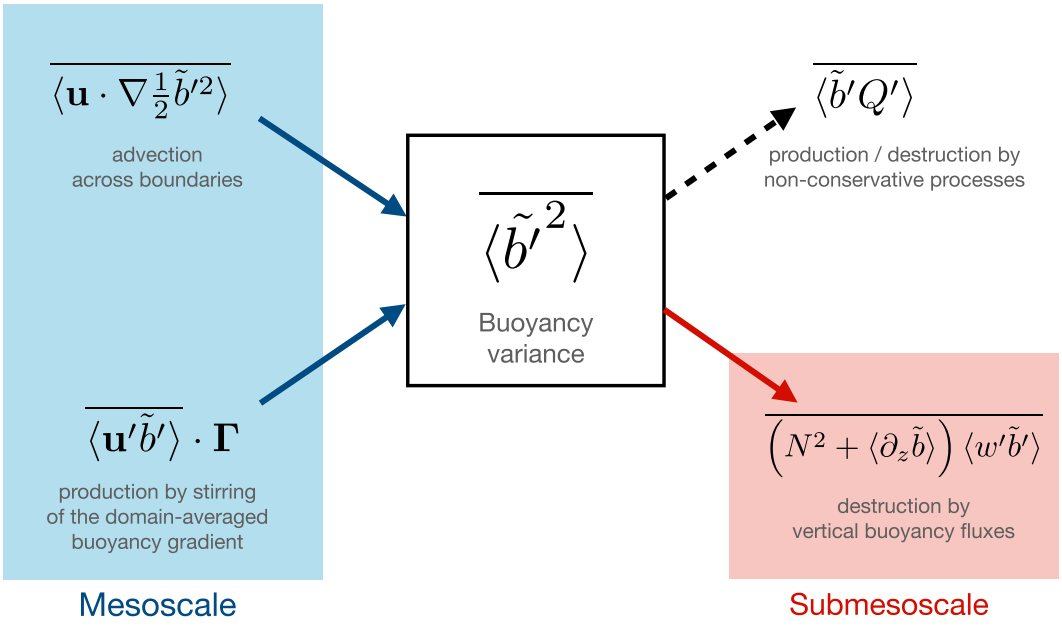

FIG. 9. Schematic of the buoyancy variance budget. Shown are all terms in (8) and an assignment of which scales are typically responsible for them. The direction of the arrows indicates whether the respective terms are sources or sinks of buoyancy variance in the upper 200 m of the analysis domain.

Wenegrat et al. (2018) applied this theoretical argument and scaling, which they calibrated using idealized simulations, to a single high-resolution realistic simulation. They filtered the surface PV fluxes in this high-resolution simulation to separate meso- and submesoscale contributions and found a vast dominance of the submesoscale part. They posited that this submesoscale contribution would be suppressed if the grid spacing was coarsened. To the degree that surface PV fluxes scale with vertical buoyancy fluxes in the mixed layer (Taylor and Ferrari 2010), the same conclusion could have been drawn from the 2-km simulation presented here (Fig. 7). Our 4- and 8-km simulations suggest, however, that this submesoscale PV injection might not have been lost at coarser resolution. Somewhat larger scales might have taken up the slack, just like we see for the vertical buoyancy flux at 4- and 8-km grid spacing (Fig. 7).

Such a behavior would violate the PV injection scaling with $\langle |\nabla b|^2 \rangle$ proposed by Wenegrat et al. (2018), because this quantity invariably increases as the resolution is increased and fronts are allowed to become sharper (Fig. 3b). We argue in the appendix that this scaling, which in Wenegrat et al.'s argument arises from separate scalings for the frictional and diabatic injection terms, does not capture the behavior of the net PV input when horizontal diffusion is varied in an Eady model. Instead, the PV input is largely invariant to how sharp fronts are allowed to become, consistent with the results of our realistic simulations. While the experiments presented in the appendix show that an increase of the PV input with $\langle |\nabla b|^2 \rangle$ is not inevitable and are instead broadly consistent with the realistic simulations presented here, these experiments are highly idealized and far from comprehensive. More work is needed to fully understand these scalings.

Applying a similar methodology as Wenegrat et al. (2018), Su et al. (2018) argued that the vertical fluxes carried by submesoscale motion are key to the heat budget of the upper ocean. They showed that the submesoscales produce a heat flux of order 100 W m^{-2} at 40-m depth. It should be noted, however, that this number was again inferred from a single high-resolution simulation using spatial filtering. Su et al. (2018) also compared simulations with different resolutions, finding the vertical heat flux to increase by 14% when the horizontal grid spacing was reduced from (1/24)° to (1/48)°. This modest increase is consistent with our simulations (Fig. 7), although it should be kept in mind that Su et al. (2018) relied on a single simulation year and a high-resolution run that was far from equilibrated.

8. Conclusions

The vertical buoyancy flux produced by submesoscale MLI can modify the stratification of the upper ocean (Boccaletti et al. 2007; Fox-Kemper et al. 2008). MLI tends to increase the stratification in the mixed layer and decrease it in the upper thermocline. The set of simulations of the subtropical North Atlantic presented in this study, however, suggests that this bulk impact of MLI, i.e., its effect on the stratification of the upper ocean through an enhanced vertical buoyancy flux, can be captured even if MLI is severely underresolved. Once mesoscale eddies are captured, the magnitude of MLI-produced vertical buoyancy fluxes is largely invariant as the submesoscales are increasingly well resolved, despite submesoscale turbulence becoming more and more energetic and producing progressively

larger vertical velocities. There is no substantial change in the vertical buoyancy flux or upper-ocean stratification when the scale of the most unstable winter MLI mode is resolved.

We emphasize that these results do not mean that the answer to the title question is "no"—an ocean with MLI has a different stratification than an ocean without. Instead, our results suggest that a merely mesoscale-resolving model does have a decent representation of the bulk effect of MLI on stratification, even if the submesoscales are severely damped.

The invariance of the buoyancy flux with increasing resolution can be understood as arising from a mesoscale constraint on the buoyancy variance budget. MLI produces an upgradient vertical buoyancy flux: an upward flux in the presence of positive stratification. This destruction of buoyancy variance is balanced by a mesoscale source of buoyancy variance, which comprises both variance import (mesoscale eddies propagating into the analysis domain) and mesoscale stirring of the large-scale lateral gradient (downgradient horizontal flux). The rate of buoyancy variance production is thus governed by mesoscale dynamics—and largely fixed once mesoscale eddies are fully resolved. Balancing this fixed production, the submesoscale variance destruction must then also be fixed. This constraint denies an increase in vertical buoyancy flux as MLI is increasingly well resolved.

If general, these results have obvious implications for global ocean models. The results suggest that resolving mesoscale eddies is sufficient to also capture the bulk effects of MLI. Mesoscale-resolving simulations should be able to capture the upper-ocean stratification and coupling, for example, between mode waters and the atmosphere. Uchida et al. (2017) indeed demonstrated that MLI develops in a 0.1° global simulation, despite being severely underresolved. The results presented here suggest that the impact of these instabilities might not have been as unrealistic as those authors suspected.

The results presented here also raise the question of whether the restratification by MLI needs to be parameterized in models that resolve mesoscale eddies (Fox-Kemper et al. 2008, 2011). If the mesoscale constraint we propose is robust and the submesoscale vertical buoyancy flux is essentially correct in mesoscale-resolving models even if the most unstable MLI mode is not resolved, the bulk effect of MLI on the stratification of the upper ocean may well be reasonably captured.

The proposed mesoscale constraint should be investigated further. The argument presented above is generic and independent of the particular region under investigation here, but an evaluation in other regions or across the World Ocean would help understand its generality. Considering this constraint in a more idealized context should also help anticipate under what conditions it might break down.

Furthermore, our simulations leave open the possibility that submesoscale processes beyond the reach of the 2-km simulation affect the large-scale structure of the ocean. On the one hand, we judge it unlikely that better resolution of summertime MLI will lead to qualitative changes, both because of the mesoscale constraint and because wintertime MLI by far dominates vertical buoyancy fluxes. On the other hand, unbalanced submesoscale instabilities, such as symmetric and inertial instabilities (e.g., Thomas et al. 2013; Gula et al. 2016), are neither captured at 2-km grid spacing nor parameterized in our simulations (cf. Bachman et al. 2017). Their potential impact on the large-scale structure of the upper ocean could not be addressed here.

In addition, the insensitivity of the buoyancy field to MLI does not necessarily imply that other tracers are not affected by progressively more energetic submesoscales. Passive tracers are typically transported down their mean gradient (including in the vertical), and tracer filamentation often implies that nonconservative processes play a leading-order role in their variance budgets. It thus seems unlikely that the mesoscale constraint described above translates into a constraint on passive-tracer fluxes. Short-term simulations suggest a strong impact on passive-tracer fluxes as submesoscales become more energetic (Balwada et al. 2018) but equilibrated simulations are needed to more fully quantify this impact. It should also be emphasized that the conclusions might depend on the mean gradients of the tracer and the phasing of these gradients with respect to wintertime MLI (Smith et al. 2016; Lévy et al. 2018).

Acknowledgments. This work was supported by the Caltech–JPL President's and Director's Research and Development Fund. AS and JC were also partially supported by NASA awards 80NM0018D0004 and 80NSSC20K1140, respectively. DM carried out the research at the Jet Propulsion Laboratory, California Institute of Technology, under a contract with NASA and with support from the Physical Oceanography (PO) and Modeling, Analysis, and Prediction (MAP) programs. The authors thank Patrice Klein for valuable discussions related to the material presented in this paper and An Nguyen for providing early access to the ASTE data. High-end computing resources for the numerical simulations were provided by the NASA Advanced Supercomputing (NAS) Division at the Ames Research Center. Marina Lévy and Jacob Wenegrat are thanked for insightful reviewer comments.

Data availability statement. The experimental setup is available at https://github.com/joernc/NA. Some of the preprocessing and analysis code can be found at https://github.com/anirban89/NorthAtlantic. Output from the simulations (incl. restart files from the equilibrated states) can be requested from the authors.

APPENDIX

Boundary PV Flux Scaling

The invariance of vertical buoyancy fluxes in the upper ocean under increases in resolution, once mesoscale eddies are fully resolved, is inconsistent with the scaling for PV injection with $|\nabla b|^2$ proposed by Wenegrat et al. (2018). As the grid spacing is refined, fronts are allowed to become sharper, and the scaling predicts the PV injection to

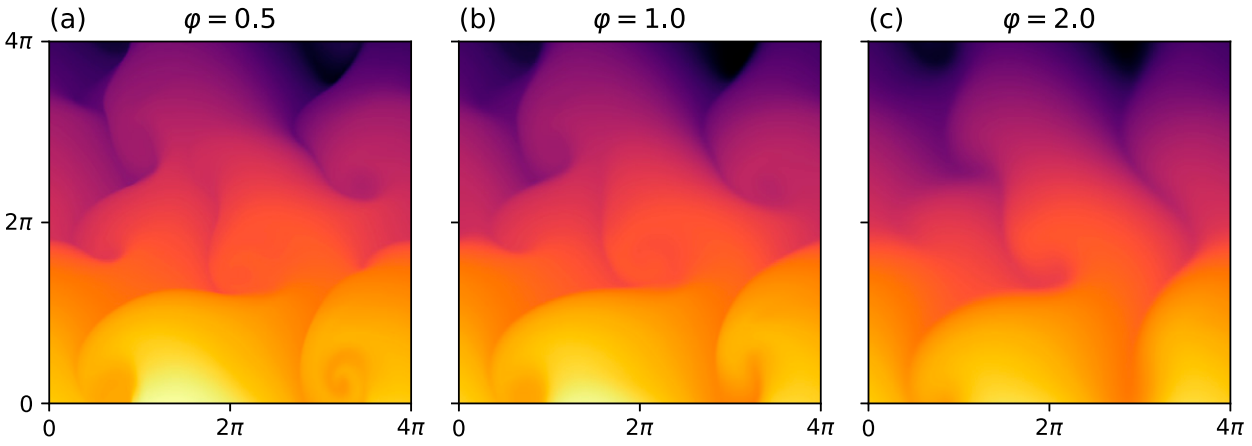

FIG. A1. Snapshots of surface buoyancy for Eady simulations with different amounts of horizontal diffusion. These snapshots show the full buoyancy $-y + b$ at time $t = 35$ with the same color scale in the three panels ($-y$ being the buoyancy of the background state). Note the reduction of buoyancy gradients with increased horizontal diffusion.

increase sharply. While we do not explicitly evaluate PV injection in the realistic simulations, it is expected to scale with the vertical buoyancy fluxes (Taylor and Ferrari 2010). To elucidate this inconsistency, we evaluate Wenegrat et al.'s scaling using an Eady model with varying horizontal diffusion to control how sharp fronts can become.

We integrate the nondimensional hydrostatic Boussinesq equations with an imposed constant background buoyancy gradient that is in thermal-wind balance with a constant zonal shear (cf. Taylor and Ferrari 2010; Callies and Ferrari 2018):

$$\partial_t u + \mathbf{u}\cdot\nabla u + z\partial_x u + w - v = -\partial_x p + \varepsilon D u, \tag{A1}$$

$$\partial_t v + \mathbf{u}\cdot\nabla v + z\partial_x v + u = -\partial_y p + \varepsilon D v, \tag{A2}$$

$$b = \partial_z p, \tag{A3}$$

$$\nabla\cdot\mathbf{u} = 0 \tag{A4}$$

$$\partial_t b + \mathbf{u}\cdot\nabla b + z\partial_x b - v = \varepsilon D b, \tag{A5}$$

where the diffusion operator $D = \varphi(\partial_{xx} + \partial_{yy}) + \partial_{zz}$ allows for an adjustment of horizontal diffusion with φ. Here, ε is the Ekman number, and the Prandtl number has been set to unity for simplicity. These equations are solved on a domain $[0,4\pi]\times[0,4\pi]\times[-1/2,1/2]$ that is periodic in both horizontal dimensions and has rigid boundaries at the top and bottom. Free-slip conditions are applied to the horizontal velocity components at the top and bottom, and $\partial_z b = 1$ is applied to maintain the initial stratification $\partial_z b = 1$ against diffusive erosion. The equations are discretized using Dedalus (Burns et al. 2020), employing 512 Fourier modes in each horizontal direction and 32 Chebyshev modes in the vertical. The integrations are initialized with small-amplitude random noise in buoyancy whose Fourier coefficients are modulated by $(\kappa_0^2 + \kappa^2)^{-3/2}$, where κ is the magnitude of the horizontal wavenumber vector and $\kappa_0 = 10$. The random seed is identical for all integrations, and the time step is 2×10^{-3}.

Integrations are performed with $\varepsilon = 10^{-2}$ and $\varphi = 0.5$, 1.0, and 2.0. The instability grows to finite amplitude and generates nonlinear baroclinic eddies (Fig. A1). Fronts form at the edges of these eddies. How strong these fronts become is controlled by the horizontal diffusion: the frontal buoyancy gradients decrease as φ is increased (Figs. A1, A2a). [See Bodner et al. (2019) for a comprehensive discussion of the effect of horizontal diffusion on frontogenesis.] Wenegrat et al.'s (2018) scaling would thus predict a decrease in PV injection as horizontal diffusion is enhanced. Once the instabilities have reached a fully nonlinear regime, that is, when the exponential growth phase has terminated, the PV input is instead comparable between the three cases (Fig. A2b).

When separated into its frictional and diabatic contributions, the magnitude of the PV input does show a clear increase with the strength of buoyancy gradients (Fig. A2c). Wenegrat et al.'s (2018) scaling may be appropriate for these individual contributions, but it appears to fail for the small residual between the two (Fig. A2b).

That the net PV input is independent of the details of the frictional and diabatic processes at the boundaries is consistent with the picture advanced by Garner et al. (1992). They showed that the PV input is similar if the instability layer is bounded by strongly stratified, high-PV layers rather than solid boundaries. In such a setup without boundaries, the PV in the instability layer increases as high-PV fluid is advected in from the adjacent strongly stratified layers, with nonconservative processes playing no significant role. In the setup with solid boundaries, the nonconservative PV fluxes that carry the PV input thus appear to be controlled by the bulk behavior of the instability, rather than controlling its bulk behavior.

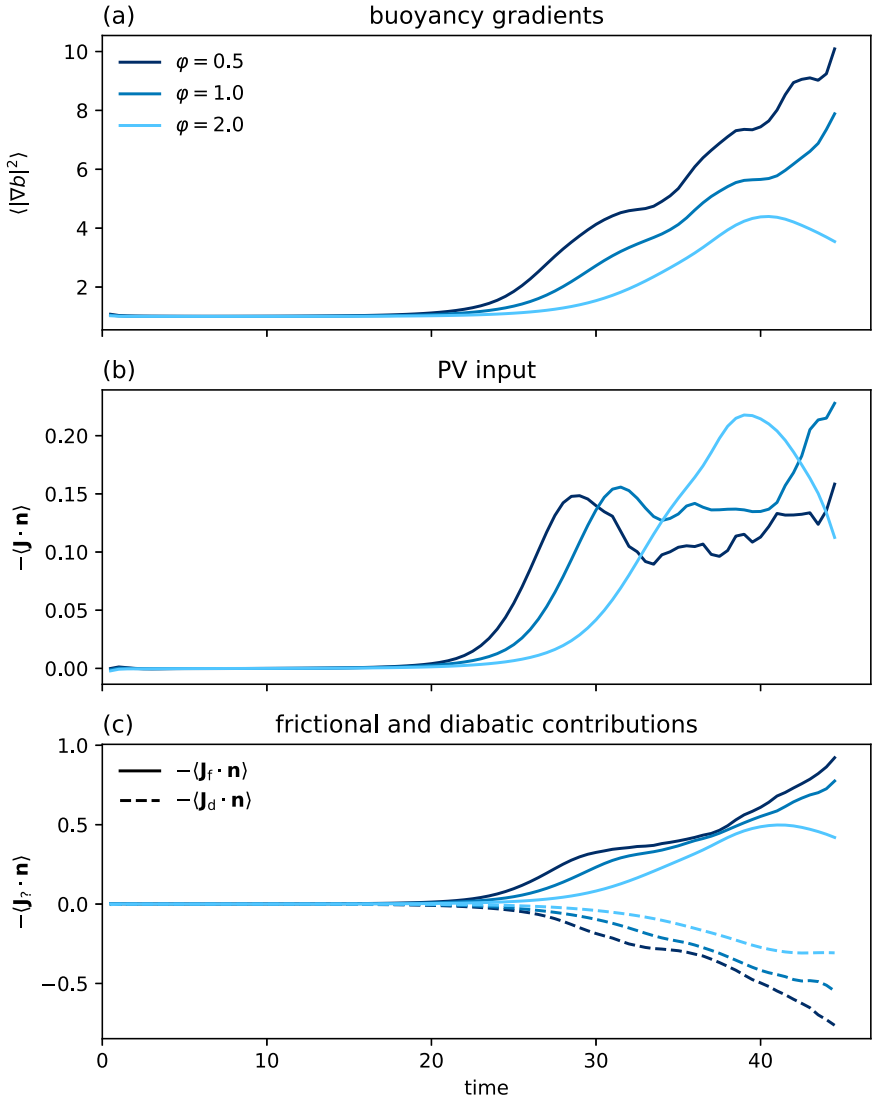

FIG. A2. Evaluation of the PV flux scaling with $|\nabla b|^2$. Shown are time series of (a) buoyancy gradients $\langle |\nabla b|^2 \rangle$, (b) the boundary PV flux $-\langle \mathbf{J} \cdot \mathbf{n} \rangle$, where $\mathbf{J}$ is the PV flux vector and $\mathbf{n}$ the unit normal of the boundary, and (c) the frictional and diabatic contributions to these boundary PV fluxes. The angle brackets here denote averages over the top and bottom boundaries.

REFERENCES

Bachman, S. D., B. Fox-Kemper, J. R. Taylor, and L. N. Thomas, 2017: Parameterization of frontal symmetric instabilities. I: Theory for resolved fronts. *Ocean Modell.*, **109**, 72–95, https://doi.org/10.1016/j.ocemod.2016.12.003.

Balwada, D., K. S. Smith, and R. Abernathey, 2018: Submesoscale vertical velocities enhance tracer subduction in an idealized Antarctic circumpolar current. *Geophys. Res. Lett.*, **45**, 9790–9802, https://doi.org/10.1029/2018GL079244.

Bates, N. R., A. C. Pequignet, R. J. Johnson, and N. Gruber, 2002: A short-term sink for atmospheric CO_2 in subtropical mode water of the North Atlantic Ocean. *Nature*, **420**, 489–493, https://doi.org/10.1038/nature01253.

Boccaletti, G., R. Ferrari, and B. Fox-Kemper, 2007: Mixed layer instabilities and restratification. *J. Phys. Oceanogr.*, **37**, 2228–2250, https://doi.org/10.1175/JPO3101.1.

Bodner, A. S., B. Fox-Kemper, L. P. Van Roekel, J. C. McWilliams, and P. P. Sullivan, 2019: A perturbation approach to understanding the effects of turbulence on frontogenesis. *J. Fluid Mech.*, **883**, A25, https://doi.org/10.1017/jfm.2019.804.

Brüggemann, N., and C. Eden, 2015: Routes to dissipation under different dynamical conditions. *J. Phys. Oceanogr.*, **45**, 2149–2168, https://doi.org/10.1175/JPO-D-14-0205.1.

Buckingham, C. E., N. S. Lucas, S. E. Belcher, T. P. Rippeth, A. L. M. Grant, J. Le Sommer, A. O. Ajayi, and A. C. Naveira Garabato, 2019: The contribution of surface and submesoscale processes to turbulence in the open ocean surface

boundary layer. *J. Adv. Model. Earth Syst.*, **11**, 4066–4094, https://doi.org/10.1029/2019MS001801.

Burns, K. J., G. M. Vasil, J. S. Oishi, D. Lecoanet, and B. P. Brown, 2020: Dedalus: A flexible framework for numerical simulations with spectral methods. *Phys. Rev. Res.*, **2**, 023068, https://doi.org/10.1103/PhysRevResearch.2.023068.

Callies, J., and R. Ferrari, 2018: Baroclinic instability in the presence of convection. *J. Phys. Oceanogr.*, **48**, 45–60, https://doi.org/10.1175/JPO-D-17-0028.1.

——, ——, J. M. Klymak, and J. Gula, 2015: Seasonality in submesoscale turbulence. *Nat. Commun.*, **6**, 6862, https://doi.org/10.1038/ncomms7862.

——, G. Flierl, R. Ferrari, and B. Fox-Kemper, 2016: The role of mixed-layer instabilities in submesoscale turbulence. *J. Fluid Mech.*, **788**, 5–41, https://doi.org/10.1017/jfm.2015.700.

——, R. Barkan, and A. N. Garabato, 2020: Time scales of submesoscale flow inferred from a mooring array. *J. Phys. Oceanogr.*, **50**, 1065–1086, https://doi.org/10.1175/JPO-D-19-0254.1.

Capet, X., J. C. McWilliams, M. J. Molemaker, and A. F. Shchepetkin, 2008: Mesoscale to submesoscale transition in the California Current system. Part I: Flow structure, eddy flux, and observational tests. *J. Phys. Oceanogr.*, **38**, 29–43, https://doi.org/10.1175/2007JPO3671.1.

Chassignet, E. P., and X. Xu, 2017: Impact of horizontal resolution (1/12° to 1/50°) on Gulf Stream separation, penetration, and variability. *J. Phys. Oceanogr.*, **47**, 1999–2021, https://doi.org/10.1175/JPO-D-17-0031.1.

Daru, V., and C. Tenaud, 2004: High order one-step monotonicity-preserving schemes for unsteady compressible flow calculations. *J. Comput. Phys.*, **193**, 563–594, https://doi.org/10.1016/j.jcp.2003.08.023.

Dong, J., B. Fox-Kemper, H. Zhang, and C. Dong, 2020: The scale of submesoscale baroclinic instability globally. *J. Phys. Oceanogr.*, **50**, 2649–2667, https://doi.org/10.1175/JPO-D-20-0043.1.

du Plessis, M., S. Swart, I. J. Ansorge, and A. Mahadevan, 2017: Submesoscale processes promote seasonal restratification in the Subantarctic Ocean. *J. Geophys. Res. Oceans*, **122**, 2960–2975, https://doi.org/10.1002/2016JC012494.

——, ——, ——, ——, and A. F. Thompson, 2019: Southern Ocean seasonal restratification delayed by submesoscale wind–front interactions. *J. Phys. Oceanogr.*, **49**, 1035–1053, https://doi.org/10.1175/JPO-D-18-0136.1.

Eady, E. T., 1949: Long waves and cyclone waves. *Tellus*, **1**, 33–52, https://doi.org/10.3402/tellusa.v1i3.8507.

Forget, G., G. Maze, M. Buckley, and J. Marshall, 2011: Estimated seasonal cycle of North Atlantic eighteen degree water volume. *J. Phys. Oceanogr.*, **41**, 269–286, https://doi.org/10.1175/2010JPO4257.1.

Fox-Kemper, B., and D. Menemenlis, 2008: Can large eddy simulation techniques improve mesoscale rich ocean models? *Ocean Modeling in an Eddying Regime*, *Geophys. Monogr.*, Vol. 177, Amer. Geophys. Union, 319–337, https://doi.org/10.1029/177GM19.

——, R. Ferrari, and R. Hallberg, 2008: Parameterization of mixed layer eddies. Part I: Theory and diagnosis. *J. Phys. Oceanogr.*, **38**, 1145–1165, https://doi.org/10.1175/2007JPO3792.1.

——, and Coauthors, 2011: Parameterization of mixed layer eddies. III: Implementation and impact in global ocean climate simulations. *Ocean Modell.*, **39**, 61–78, https://doi.org/10.1016/j.ocemod.2010.09.002.

Fukumori, I., O. Wang, I. Fenty, G. Forget, P. Heimbach, and R. M. Ponte, 2020: Synopsis of the ECCO central production global ocean and sea-ice state estimate, version 4 release 4. Zenodo, accessed 1 February 2021, https://doi.org/10.5281/zenodo.3765929.

Garner, S. T., N. Nakamura, and I. M. Held, 1992: Nonlinear equilibration of two-dimensional Eady waves: A new perspective. *J. Atmos. Sci.*, **49**, 1984–1996, https://doi.org/10.1175/1520-0469(1992)049<1984:NEOTDE>2.0.CO;2.

Garrett, C., and W. H. Munk, 1972: Space-time scales of internal waves. *Geophys. Fluid Dyn.*, **3**, 225–264, https://doi.org/10.1080/03091927208236082.

Gula, J., M. J. Molemaker, and J. C. McWilliams, 2014: Submesoscale cold filaments in the Gulf Stream. *J. Phys. Oceanogr.*, **44**, 2617–2643, https://doi.org/10.1175/JPO-D-14-0029.1.

——, ——, and ——, 2016: Topographic generation of submesoscale centrifugal instability and energy dissipation. *Nat. Commun.*, **7**, 12811, https://doi.org/10.1038/ncomms12811.

Hersbach, H., and Coauthors, 2020: The ERA5 global reanalysis. *Quart. J. Roy. Meteor. Soc.*, **146**, 1999–2049, https://doi.org/10.1002/qj.3803.

Iudicone, D., K. B. Rodgers, Y. Plancherel, O. Aumont, T. Ito, R. M. Key, G. Madec, and M. Ishii, 2016: The formation of the ocean's anthropogenic carbon reservoir. *Sci. Rep.*, **6**, 35473, https://doi.org/10.1038/srep35473.

Jackett, D. R., and T. J. McDougall, 1995: Minimal adjustment of hydrographic profiles to achieve static stability. *J. Atmos. Oceanic Technol.*, **12**, 381–389, https://doi.org/10.1175/1520-0426(1995)012<0381:MAOHPT>2.0.CO;2.

Karleskind, P., M. Levy, and L. Memery, 2011: Modifications of mode water properties by sub-mesoscales in a bio-physical model of the northeast Atlantic. *Ocean Model.*, **39**, 47–60, https://doi.org/10.1016/j.ocemod. 2010.12.003.

Kwon, Y.-O., and S. C. Riser, 2004: North Atlantic subtropical mode water: A history of ocean-atmosphere interaction 1961–2000. *Geophys. Res. Lett.*, **31**, L19307, https://doi.org/10.1029/2004GL021116.

Large, W. G., and A. J. G. Nurser, 2001: Ocean surface water mass transformation. *Ocean Circulation and Climate: Observing and Modeling the Global Ocean*, G. Siedler, J. Church, and J. Gould, Eds., International Geophysics Series, Vol. 77, Academic Press, 317–336, http://nora.nerc.ac.uk/154885/.

——, J. C. McWilliams, and S. C. Doney, 1994: Oceanic vertical mixing: A review and a model with a nonlocal boundary layer parameterization. *Rev. Geophys.*, **32**, 363–403, https://doi.org/10.1029/94RG01872.

Lévy, M., P. Klein, A.-M. Tréguier, D. Iovino, G. Madeca, S. Massona, and K. Takahashic, 2010: Modifications of gyre circulation by sub-mesoscale physics. *Ocean Modell.*, **34**, 1–15, https://doi.org/10.1016/j.ocemod.2010.04.001.

——, P. J. S. Franks, and K. S. Smith, 2018: The role of submesoscale currents in structuring marine ecosystems. *Nat. Commun.*, **9**, 4758, https://doi.org/10.1038/s41467-018-07059-3.

Luyten, J. R., J. Pedlosky, and H. Stommel, 1983: The ventilated thermocline. *J. Phys. Oceanogr.*, **13**, 292–309, https://doi.org/10.1175/1520-0485(1983)013%3C0292:TVT%3E2.0.CO;2.

Marshall, D., 1997: Subduction of water masses in an eddying ocean. *J. Mar. Res.*, **55**, 201–222, https://doi.org/10.1357/0022240973224373.

Marshall, J., A. Adcroft, C. Hill, L. Perelman, and C. Heisey, 1997: A finite-volume, incompressible Navier Stokes model for studies of the ocean on parallel computers. *J. Geophys. Res.*, **102**, 5753–5766, https://doi.org/10.1029/96JC02775.

——, H. Jones, R. Karsten, and R. Wardle, 2002: Can eddies set ocean stratification? *J. Phys. Oceanogr.*, **32**, 26–38, https://doi.org/10.1175/1520-0485(2002)032<0026:CESOS>2.0.CO;2.

Mensa, J. A., Z. Garraffo, A. Griffa, T. M. Özgökmen, A. Haza, and M. Veneziani, 2013: Seasonality of the submesoscale dynamics in the Gulf Stream region. *Ocean Dyn.*, **63**, 923–941, https://doi.org/10.1007/s10236-013-0633-1.

Nakamura, N., and I. M. Held, 1989: Nonlinear equilibration of two-dimensional Eady waves. *J. Atmos. Sci.*, **46**, 3055–3064, https://doi.org/10.1175/1520-0469(1989)046<3055:NEOTDE>2.0.CO;2.

Nguyen, A. T., H. Pillar, V. Ocaña, A. Bigdeli, T. A. Smith, and P. Heimbach, 2021: The Arctic Subpolar gyre sTate Estimate (ASTE): Description and assessment of a data-constrained, dynamically consistent ocean-sea ice estimate for 2002–2017. *J. Adv. Model. Earth Syst.*, **13**, e2020MS002398, https://doi.org/10.1029/2020MS002398.

Palter, J. B., M. S. Lozier, and R. T. Barber, 2005: The effect of advection on the nutrient reservoir in the North Atlantic subtropical gyre. *Nature*, **437**, 687–692, https://doi.org/10.1038/nature03969.

Renault, L., M. J. Molemaker, J. Gula, S. Masson, and J. C. McWilliams, 2016: Control and stabilization of the Gulf Stream by oceanic current interaction with the atmosphere. *J. Phys. Oceanogr.*, **46**, 3439–3453, https://doi.org/10.1175/JPO-D-16-0115.1.

Sasaki, H., P. Klein, B. Qiu, and Y. Sasai, 2014: Impact of oceanic-scale interactions on the seasonal modulation of ocean dynamics by the atmosphere. *Nat. Commun.*, **5**, 5636, https://doi.org/10.1038/ncomms6636.

——, ——, Y. Sasai, and B. Qiu, 2017: Regionality and seasonality of submesoscale and mesoscale turbulence in the North Pacific Ocean. *Ocean Dyn.*, **67**, 1195–1216, https://doi.org/10.1007/s10236-017-1083-y.

Schubert, R., J. Gula, R. J. Greatbatch, B. Baschek, and A. Biastoch, 2020: The submesoscale kinetic energy cascade: Mesoscale absorption of submesoscale mixed layer eddies and frontal downscale fluxes. *J. Phys. Oceanogr.*, **50**, 2573–2589, https://doi.org/10.1175/JPO-D-19-0311.1.

Smith, K. M., P. E. Hamlington, and B. Fox-Kemper, 2016: Effects of submesoscale turbulence on ocean tracers. *J. Geophys. Res. Oceans*, **121**, 908–933, https://doi.org/10.1002/2015JC011089.

Stammer, D., K. Ueyoshi, A. Köhl, W. G. Large, S. A. Josey, and C. I. Wunsch, 2004: Estimating air-sea fluxes of heat, freshwater, and momentum through global ocean data assimilation. *J. Geophys. Res.*, **109**, C05023, https://doi.org/10.1029/2003JC002082.

Stone, P. H., 1966: On non-geostrophic baroclinic stability. *J. Atmos. Sci.*, **23**, 390–400, https://doi.org/10.1175/1520-0469(1966)023<0390:ONGBS>2.0.CO;2.

Su, Z., J. Wang, P. Klein, A. F. Thompson, and D. Menemenlis, 2018: Ocean submesoscales as a key component of the global heat budget. *Nat. Commun.*, **9**, 775, https://doi.org/10.1038/s41467-018-02983-w.

Taylor, J. R., and R. Ferrari, 2010: Buoyancy and wind-driven convection at mixed layer density fronts. *J. Phys. Oceanogr.*, **40**, 1222–1242, https://doi.org/10.1175/2010JPO4365.1.

——, S. Bachman, M. Stamper, P. Hosegood, K. Adams, J.-B. Sallee, and R. Torres, 2018: Submesoscale Rossby waves on the Antarctic circumpolar current. *Sci. Adv.*, **4**, eaao2824, https://doi.org/10.1126/sciadv.aao2824.

Thomas, L. N., J. R. Taylor, R. Ferrari, and T. M. Joyce, 2013: Symmetric instability in the Gulf Stream. *Deep-Sea Res. II*, **91**, 96–110, https://doi.org/10.1016/j.dsr2.2013.02.025.

Thompson, A. F., A. Lazar, C. Buckingham, A. C. Naveira Garabato, G. M. Damerell, and K. J. Heywood, 2016: Open-ocean submesoscale motions: A full seasonal cycle of mixed layer instabilities from gliders. *J. Phys. Oceanogr.*, **46**, 1285–1307, https://doi.org/10.1175/JPO-D-15-0170.1.

Uchida, T., R. Abernathey, and S. Smith, 2017: Seasonality of eddy kinetic energy in an eddy permitting global climate model. *Ocean Modell.*, **118**, 41–58, https://doi.org/10.1016/j.ocemod.2017.08.006.

Wenegrat, J. O., L. N. Thomas, J. Gula, and J. C. McWilliams, 2018: Effects of the Submesoscale on the potential vorticity budget of ocean mode waters. *J. Phys. Oceanogr.*, **48**, 2141–2165, https://doi.org/10.1175/JPO-D-17-0219.1.

Worthington, L. V., 1958: The 18° water in the Sargasso Sea. *Deep-Sea Res.*, **5**, 297–305, https://doi.org/10.1016/0146-6313(58)90026-1.